MIT Open Access Articles

Novel Channel-type Heat Exchanger for a Megawatt-Class Integrated Motor Drive Technology Demonstrator

Massachusetts Institute of Technology

Novel Channel-type Heat Exchanger for a Megawatt-Class Integrated Motor Drive Technology Demonstrator

Yuankang Chen*, Zoltán S. Spakovszky†, Edward M. Greitzer‡, Zachary C. Cordero§,
David G. Cuadrado¶, Charlotte H. Gump‖, and Marc Amato**
Massachusetts Institute of Technology, Gas Turbine Laboratory, Cambridge, MA, 02139

A compact, high-performance heat exchanger is critical to realizing high specific power megawatt-class electric machines, but the combined structural and thermal performance requirements are challenging for both lattice and fin-type architectures. A novel channel-type architecture, enabled by advances in additive manufacturing techniques, is proposed to address this need. The scale of the application limits heat exchanger operation to transition regime, and surface roughness is identified as a critical performance parameter. The structural and thermal performance of the optimized heat exchanger is assessed in CFD and FEA to meet requirements, and experimentally validated under representative torque and flow conditions.

I. Nomenclature

d_H	=	hydraulic diameter
k_s	=	sand-grain roughness
k_τ	=	torsional stiffness
r	=	radius
l	=	heat exchanger length
R_θ	=	thermal resistance
α	=	coefficient of linear thermal expansion
Nu	=	Nusselt number
Re	=	Reynolds number
h	=	heat transfer coefficient
k	=	thermal conductivity
t	=	thickness
T	=	torque
θ	=	angular displacement

II. Introduction

Heat exchangers promote heat transfer and reduce overall thermal resistance by increasing the surface area available for cooling. Advances in additive manufacturing have enabled not only smaller and more compact heat exchangers, but also improved convective heat transfer coefficients through novel features (e.g. vortex generators) and new lattice architectures[1].

In addition to stringent thermal performance requirements, the heat exchanger of the megawatt-class integrated motor drive [2] is subject to significant structural loading. To minimize system mass, the heat exchanger is used as a structural element, transmitting torque from the machine stator to the machine frame. Mitigating the risk of core-heat exchanger separation during operation due to differential thermal growth requires an interference fit, which imposes compressive loads on the heat exchanger outer surface. Conventional fin-type architectures are vulnerable to buckling

---

*Research Assistant, now working at GE Global Research

†T.A. Wilson Professor of Aeronautics and Astronautics; Head, Air Sector; Director, Gas Turbine Laboratory, 31-317

‡H.N. Slater Professor of Aeronautics and Astronautics, 31-319

§Assistant Professor of Aeronautics and Astronautics, 33-332

¶Research Engineer, 31-316

‖Undergraduate Research Assistant, AeroAstro

**CEO,Innova-Logic LLC, Saunderstown, RI, 02874

under the combined loads. New foam or 'lattice-type' architectures are structurally resilient with modest convective heat transfer capability[3], but do not propagate heat through their structures well (having a comparatively low 'fin efficiency'). The proposed channel-type heat exchanger architecture leverages additive manufacturing techniques to blend both architectures and meet the combined structural and thermal requirements.
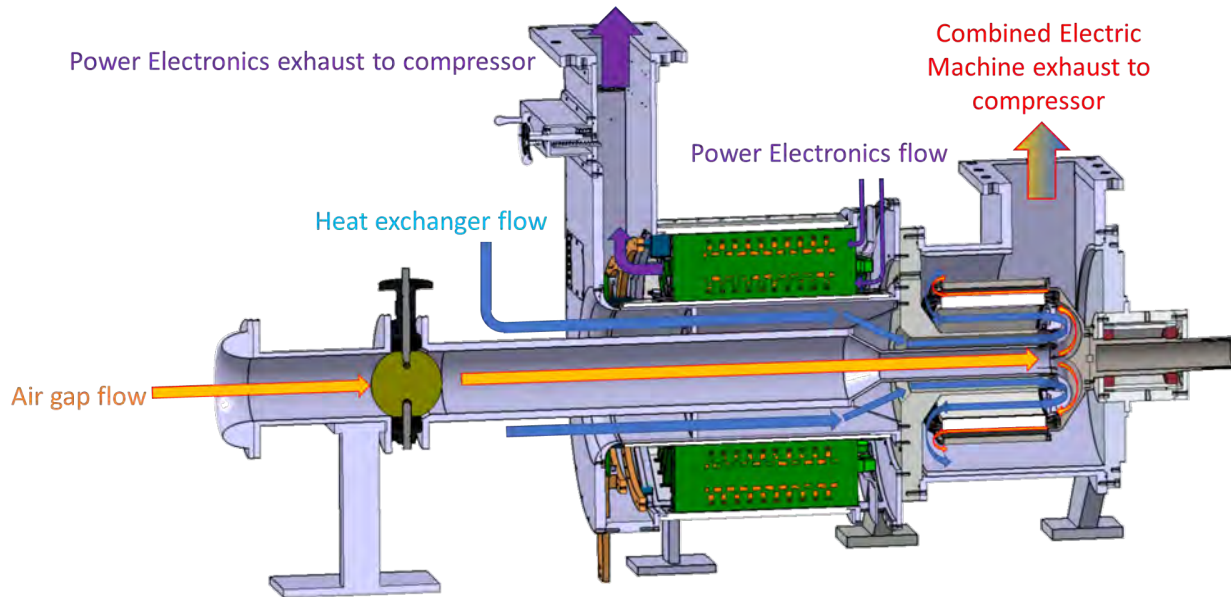

Fig. 1   Air cooling system of the 1 MW motor drive demonstrator [2]

A heat exchanger design framework utilizing reduced order models and empirical correlations for friction factor and Nusselt number [4] is developed to identify the optimum design with minimum thermal resistance through an exploration of the design space. The optimum geometry is found to depend strongly on channel surface roughness, as system cooling flow limits constrain operation to the flow transition regime. Predicting surface roughness in additively-manufactured thin-walled structures is an ongoing field of study [5], and the thin wall thickness, small size (hydraulic diameters on the order of 1 mm), and high length-to-hydraulic diameter aspect ratio of the channels present significant barriers to controlling surface roughness via finishing processes such as polishing. As a risk mitigation measure, several 1-inch tall sections of the heat exchanger were printed and their surface roughness measured. These sections are printed together with the full-size heat exchangers, in identical print orientation and beam settings, and surface metrology of these sections confirms that surface roughness matches design assumptions.

A set of torque-loading and thermal performance characterization experiments was conducted on the final heat exchanger to validate that it meets design requirements. The heat exchanger was torsionally loaded up to 112% of operating load over five cycles, and no signs of damage were observed. The thermal resistance of the final heat design is estimated via experimental measurements at 0.0059 K/W, 17% lower than the maximum allowed value of 0.0071 K/W, and will enable the demonstrator to be operated at 21°C below the winding hotspot temperature limit at design.

Differential thermal expansion of the core and heat exchanger presents a risk of interface separation during operation. This would result in a loss of torque transfer capability and structural damage to the motor, and significantly reduced heat transfer capability due to the creation of an insulating air gap between the stator and the heat exchanger. Therefore, the core-heat exchanger interface is designed for a nominal 5 thou interference fit, larger than the estimated 3 thou thermal differential growth between heat exchanger OD and core ID during operation. The choice of this interference fit magnitude is determined after assessing the various safety margins that trade off against one another (e.g. structural integrity vs thermal). Structural loading challenges associated with the interference fit will likely increase as electric machine designs become increasingly compact, and anti-buckling features such as those of the channel-type architecture will be an important measure to address them.

III. Heat Exchanger Design

A. Heat Exchanger Design Requirements

- **Structural Integrity:** The heat exchanger is used as a structural element, and thus must be capable of withstanding combined loads from the design torque of 765 Nm, the weight of the electric machine stator, and any compressive loads from an interference fit.
- **Thermal Performance:** To keep the winding hotspot below the insulation temperature limit of 180°C, the heat exchanger thermal resistance cannot exceed 0.0071 K/W. The heat exchanger thermal resistance is defined as the temperature difference between maximum core inner surface temperature and coolant inlet temperature divided by total heat transferred through the heat exchanger. This includes the interfacial thermal resistance between the core and the heat exchanger.

An aluminum alloy (A205) is selected for the heat exchanger material to minimize mass while meeting the combined structural and thermal performance requirements.

B. Heat Exchanger Architectures

Figure 2 illustrates the three different heat exchanger architectures explored:

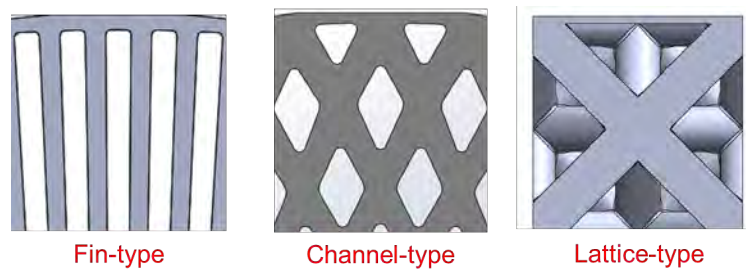Fin-type   Channel-type   Lattice-type

Fig. 2 Heat Exchanger Architectures

The conventional fin-type architecture is susceptible to buckling induced by the combination of compressive loads from the interference fit and bending loads from torque. Figure 3 shows a fin-type heat exchanger buckling under combined loading, and a channel-type heat exchanger (HEX) with comparable solidity* (and hence mass) capable of the same loads.
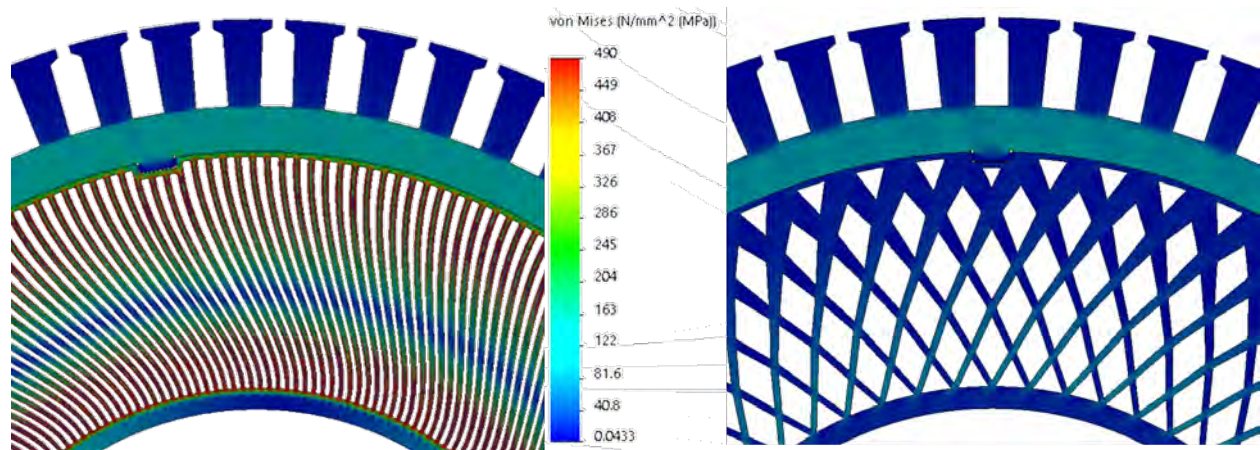

Fig. 3 Fin-type (left) and channel-type (right) under combined torque and compressive loads

The lattice-type architecture has struts in three directions providing structural resilience to torque loading. The struts of the lattice promote turbulent flow and correspondingly comparatively higher convective heat transfer coefficients,

---

*Solidity is defined as the fraction of the heat exchanger (excluding inner and outer walls) that is solid.

and should therefore in theory provide superior thermal performance to the fin-type. Hwang et al [3] experimentally characterized a set of foams with various porosities and found them to have modest convective heat transfer capability, with pore Nusselt numbers ~10. However, there is limited analysis on the scalability of these foams, or how they compare against fin-type architectures under equivalent geometric and mass constraints. One critical concern is how the overall heat transfer capability scales with foam height - if the lattice structure conduct heat well enough to retain a high 'fin efficiency'.

A design space exploration of fin-type and lattice-type heat exchangers with reduced order models is conducted to assess the comparative thermal performance of the lattice-type architecture for the demonstrator scale, with the heat exchanger thermal resistance as the performance metric. The heat exchanger design constraints for the demonstrator application are a combination of geometry (outer radius of 129 mm and overall length of 152 mm) and flow limits (maximum allowable pressure drop of 14.2 kPa and maximum mass flow of 0.706 kg/s)[†]. The design variables are nondimensional heat exchanger thickness (defined as the heat exchanger radial thickness divided by the outer radius), solidity, and number of fins (for the fin-type) or lattice cell size (for the lattice-type). For each heat exchanger geometry, the thermal resistance and pressure drop for a range of mass flows is calculated[‡].

Results of the design space exploration are presented in Figures 4 and 5, with each point on a chart representing the minimum thermal resistance for a unique fin-type or lattice-type heat exchanger geometry operating under the specified flow constraints. Figure 4 shows that under identical constraints, the thermal resistance of the lattice-type is significantly higher than that of the fin-type. While the Nusselt number and hence the heat transfer coefficient is indeed superior in the lattice-type due to the turbulent flow promoted by its struts (Figure 5), heat cannot effectively conduct through the lattice structure, as evidenced by its significantly lower 'fin efficiency'[§]. The cause of the poor efficiency is identified to be the joints of the struts, which act as thermal 'choke points' where the total cross-sectional area of the struts reaches a minimum. Figure 6 shows the temperature distribution in a cuboid section of an octet-truss lattice structure assessed in CFD. The largest temperature drops (reflected as sharp color gradients) correspond to large local thermal resistance, and occur in the direct vicinity of the strut joints.
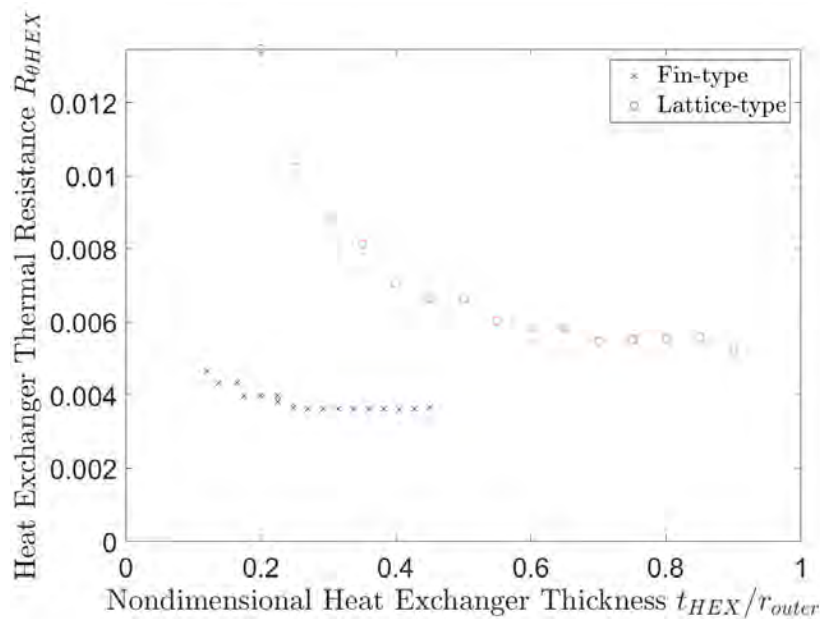

Fig. 4   Fin-type consistently outperforms lattice-type on thermal resistance due to superior fin efficiency

The channel-type architecture can be arrived at by modifying the fin-type with two opposing sets of angled, intersecting fins, which places the slender fins in compression and tension loads in response to torque loads (as opposed to bending). Alternatively, it can also be arrived at from the lattice-type by improving heat propagation through the

---

[†]These constraints are representative of, but not exactly equal to, that of the final heat exchanger of the demonstrator.

[‡]Details of the empirical models for the heat exchanger heat transfer and pressure drop coefficients can be found in Appendix C.

[§]Fin efficiency is defined as convective resistance divided by total thermal resistance, with high fin efficiency implying that heat is being effectively conducted through the solid structure.
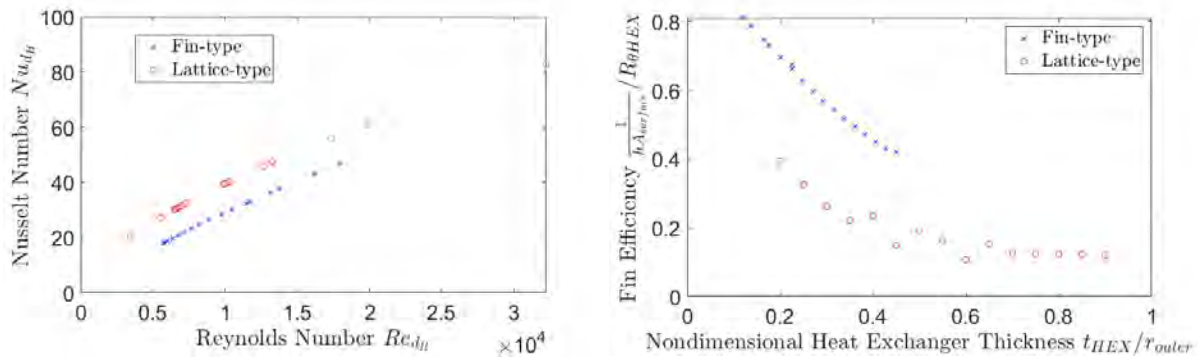
Fig. 5   Lattice-type yields superior Nu to Fin-type as struts promote turbulent flow but poorer fin efficiency
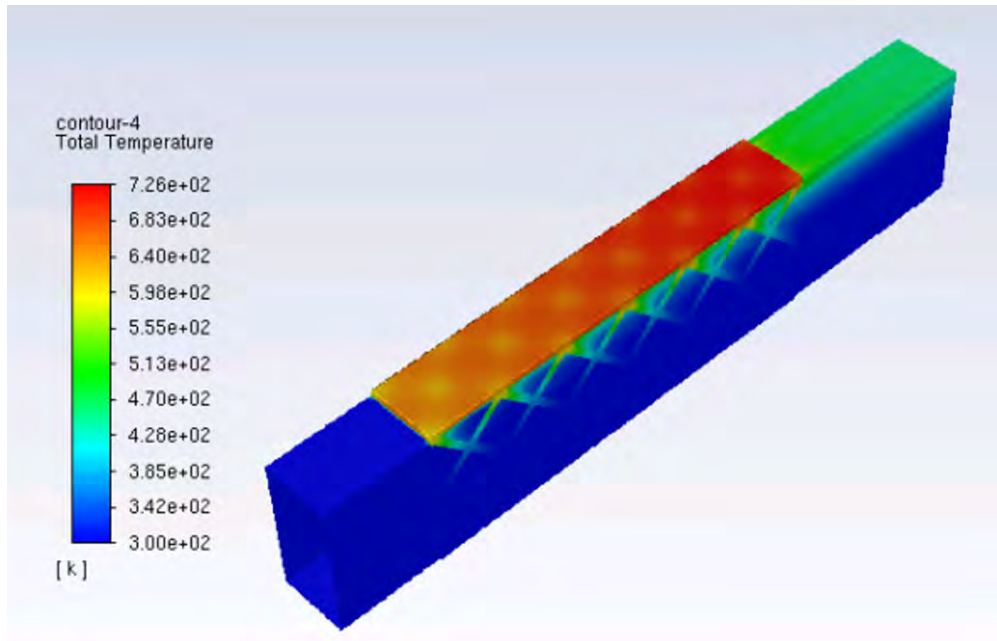

Fig. 6   Strut joints act as 'thermal chokepoints', limiting heat conduction through lattice structure

lattice structure with the removal of the horizontal strut members and thickening the remaining struts in the direction of flow (until they merge and become fins). Convective heat transfer in the channel-type architecture is dominated by pipe flow, and it is expected that the channel-type retains much of the overall heat transfer capability of the fin-type. The fillets at the intersections of the curved fins minimize reductions in fin cross-sectional area, avoiding the loss in fin efficiency observed in the lattice-type.

C. Heat Exchanger Design Optimization

A heat exchanger design framework utilizing reduced order models and empirical correlations for friction factor and Nusselt number [4] is developed to identify the final heat exchanger design. A design sweep across a range of design parameters including solidity, fin angle, surface roughness, and channel size (hydraulic diameter) is then conducted with this framework to identify the optimum design with minimum thermal resistance. The thermal resistance of the final design is estimated via CFD at 0.0057 K/W, 20% lower than the maximum allowed value of 0.0071 K/W, and would enable the demonstrator to operate at 20°C below the winding hotspot temperature limit at design.

5

1. Key Design Parameter: Relative Surface Roughness

Increasing surface roughness typically improves heat transfer (via turbulent mixing) at the cost of increased flow pressure losses. However, the demonstrator heat exchanger is constrained by physical size and allowable coolant mass flow to operation in the flow transition regime, which limits the performance benefits from high surface roughness.

Flow experiments conducted with an additively-manufactured aluminum fin-type prototype heat exchanger illustrate the challenge associated with surface roughness. Figure 8 plots the skin friction factor estimated via empirical correlations, CFD, and experiments against channel Reynolds Number on a chart from Nikuradse [6]. The range of Reynolds numbers encompassed in the analysis (3000-6000) reflect the heat exchanger mass flows achieved in the experiment, with a Re of 6000 corresponding to a mass flow of 0.58 kg/s.
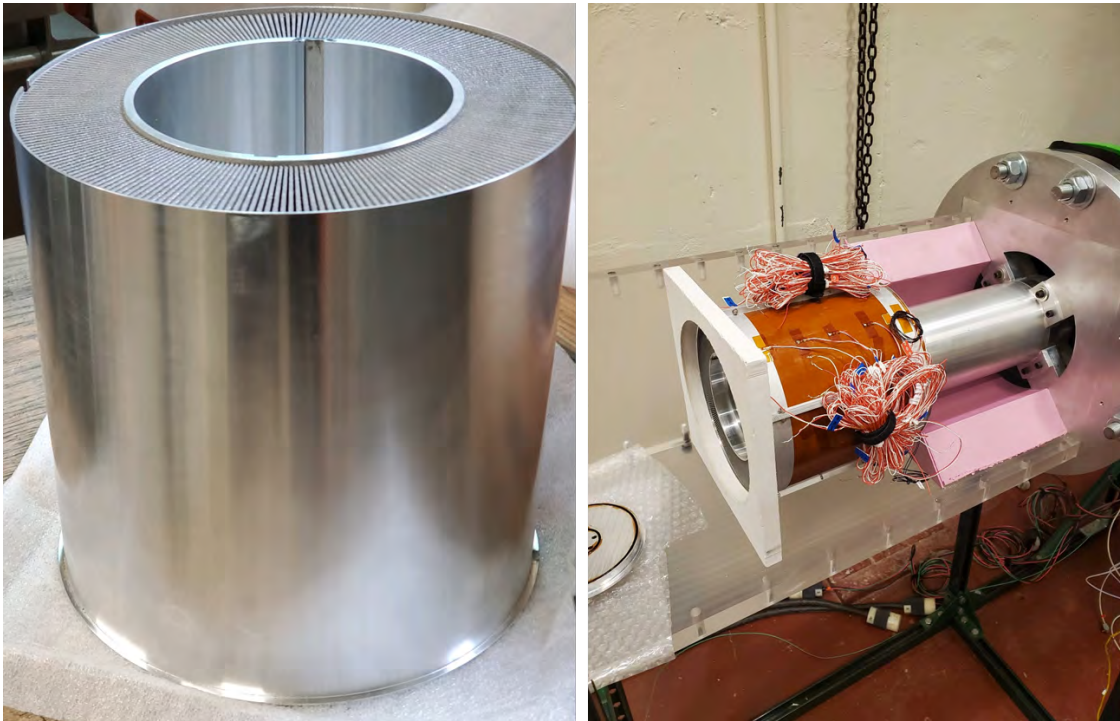

Fig. 7   Fin-type prototype (left) and hot flow experiment setup (right)

The fin-type prototype has a measured fin surface roughness $R_{zd} = 199\mu m$, corresponding to a sand grain roughness of $k_s = 195\mu m$. Compared against the channel hydraulic diameter of $d_H = 2.48$ mm, the fin-type has a relative roughness of $r/k_s = 6.28$, which is outside the bounds of Nikuradse's data [6]. The friction factor predicted by the empirical correlations (and the CFD calculations that utilize these correlations) are thus extrapolations, which is likely why they diverge by 2-3x from the experiment estimates. The underestimation of pressure losses in heat exchangers with high relative roughnesses, together with the increasing friction factor with Reynolds Number in the transition regime, presents a risk of making the design cooling mass flow unachievable.

It is conjectured that the impact of the reduced achievable mass flow on the heat exchanger's thermal performance should be partially offset by the improved heat transfer coefficient from the increased friction factor. However, hot flow experiments on the fin-type show that the heat transfer (characterized by Nusselt number Nu) is similarly overestimated by the empirical correlations.

Figure 9 plots the experimental estimates of Nusselt number against various empirical correlations. The experimental estimates for channel-average Nu are calculated by mapping the measured heat exchanger thermal resistance to FEA calculations with various values of uniform Nu. The Gnielinski correlations accounting for surface roughness are found to overestimate Nu by a factor of 4. Additionally, the sensitivity of Nu to Re is far lower than expected, even compared to the smooth-wall correlations. This reduced sensitivity could be explained if that flow in the comparatively long and narrow ($l/d_H \approx 100$) channel becomes fully developed somewhere within the heat exchanger, at which point the Nusselt number becomes invariant to Reynolds number.
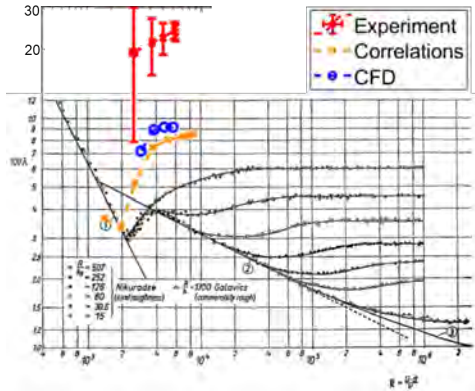
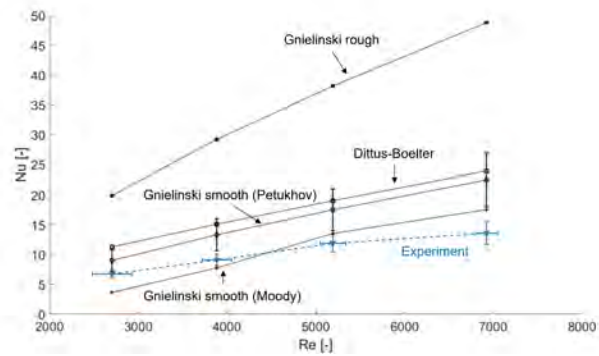**Fig. 8   Friction factor significantly under-estimated with extrapolated correlations**

Fig. 9   Experimentally-estimated Nusselt number compares poorly with various empirical correlations

D. Final Heat Exchanger Design

Figure 10 shows the final, optimized, heat exchanger design, with an average channel hydraulic diameter of 3.1 mm. The interfacial thermal resistance is estimated at 0.020 K/W based on an assumed thermal contact conductance of 3800 W/m^2K for steel-aluminum.
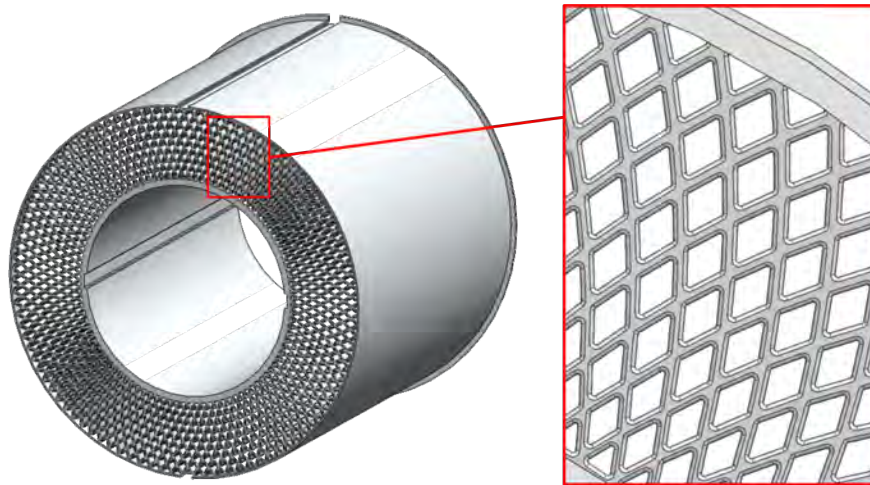

Fig. 10   Final heat exchanger geometry optimized for minimum thermal resistance

The total thermal resistance of this geometry at nominal operating conditions is estimated via CFD at 0.0057 K/W, 27% lower than the limit of 0.0071 K/W, and is estimated to enable the windings to operate at 23°C below temperature limits at design. 2D thermal FEA results showed a differential thermal growth between the core and heat exchanger of 3 thou during operation. After considering the variation in interference fit of ±1 thou due to machining tolerances, a nominal interference fit of 5 thou is selected to balance the structural safety factor of the core and the risk of thermal separation. 2D structural FEA showed the heat exchanger to have a structural safety factor of 3 under combined loading.

As part of quality control processes, 1-inch tall 18-degree sections of the heat exchanger were printed and their surface roughness measured. These sections are printed together with the full-size heat exchangers, in identical print orientation and beam settings. Figure 11 shows the test section on top with several pieces cut away to allow measurement of the roughness of the internal (channel) surfaces. Figure 12 shows the two channel surfaces measured and the optical profilometry results. The measured surface roughness (Ra) of sample 1 was 415 μin, and 372 μin for sample 2. These measurements closely match the assumed value of 350 μin from the manufacturer's specifications, suggesting the convective heat transfer should match predictions.

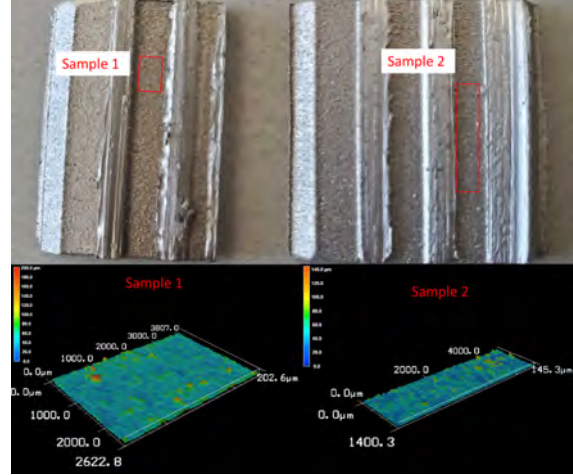**Fig. 11 Heat exchanger sample sections for surface metrology assessment**

Fig. 12 Heat exchanger optical profilometry results show measured surface roughness match design assumptions closely

IV. Choice of Core-Heat Exchanger Interference Fit

A. Challenge: Differential Thermal Growth

The relative position of the heat exchanger and core (the heat load) in the outer rotor machine architecture poses a catastrophic risk that the stator will thermally accelerate away from the heat exchanger during operation due to a differential thermal growth of both components during operation. This loss in physical contact between would result in a loss of torque transfer capability (and hence structural damage to the motor drive), and a loss of heat transfer capability due to the creation of an insulating air gap between the stator and the heat exchanger (resulting in thermal failure). Consider an idealized stator (shown in Figure 13) consisting of two concentric cylinders: a core radially outward of and in contact with a heat exchanger. Heat is generated in the core, and transferred radially inward to the heat exchanger, where it is then removed by a cooling flow.
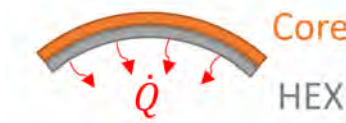

Fig. 13 Idealized stator model for differential thermal growth analysis

Assuming the core and heat exchanger have infinite thermal conductivity (and are thus individually at uniform temperature), for some heat generation $\dot{Q}$, the temperatures of the two components are:

$$T_{core} = T_{HEX} + \frac{\dot{Q}}{h_{c,int} A_{int}} = T_{HEX} + \frac{\dot{\phi}_q}{h_{int}} \tag{1}$$

$$T_{HEX} = T_0 + \dot{Q} R_{\theta,HEX} \tag{2}$$

where the subscripts $core$, HEX, and 0 refer to the core, heat exchanger, and ambient conditions respectively. h_{int} and A_{int} are the interfacial thermal conductance and contact area respectively, and $\phi_q = \frac{\dot{Q}}{A_{int}}$ is the interfacial heat flux. $R_{\theta,HEX}$ is the thermal resistance of the heat exchanger (excluding the interfacial contact resistance). Assuming both components start from ambient temperature T_0, the thermal growth of each component is:

$$\frac{\Delta r_{core}}{r_{core}} = \alpha_{core}(T_{core} - T_0) \tag{3}$$

8

$$\frac{\Delta r_{HEX}}{r_{HEX}} = \alpha_{HEX}(T_{HEX} - T_0) \tag{4}$$

where α is the coefficient of linear thermal expansion (CTE) for each material. Assuming the heat exchanger and core are sufficiently thin ($r_{core} \approx r_{HEX}$), the nondimensional differential thermal growth of the stator is:

$$\begin{aligned}\frac{\Delta r_{core} - \Delta r_{HEX}}{r_{HEX}} &= \alpha_{core}(T_{core} - T_0) - \alpha_{HEX}(T_{HEX} - T_0) \\ &= \alpha_{core} T_0 \Big[\frac{\dot{\phi}_q}{h_{c,int} T_0} + (1 - \frac{\alpha_{HEX}}{\alpha_{core}})(1 + \frac{\dot{Q} R_{\theta,HEX}}{T_0}) \Big] \end{aligned} \tag{5}$$

Equation 5 shows the parameters that set the differential thermal growth, and the limited controls managing it. As electric machine specific power improves and machines become more compact, heat flux $\dot{\phi}_q$ typically increases as the reduction in machine size is not accompanied by a proportional decrease in losses.

Interfacial thermal conductance $h_{c,int}$ can be improved through a combination of smooth contact surfaces and a high contact pressure. Increasing contact pressure comes at the cost of increased structural loads (hoop stress in the core and compressive buckling stresses in the heat exchanger for an outer-rotor architecture).

An appropriate CTE ratio $\frac{\alpha_{HEX}}{\alpha_{core}}$ could entirely eliminate or reverse the differential thermal growth. However, CTE is a material property, and freedom in material selection is typically tightly constrained as other material property requirements tend to dominate (electromagnetic performance for the core and thermal conductivity and structural strength for the heat exchanger).

B. Selection of Design Interference Fit

The stator is designed with an interference fit to prevent interface separation. The magnitude of interference fit is selected to balance the following performance metrics:

- **Structural Safety Factor (SF)** Structural safety factor is the material yield strength divided by the peak stress. Two loading conditions are considered - the cold (room temperature) state, which sees the highest stresses from the interference fit, and the operating state, at design temperature and design torque load. The minimum safety factor between the core and the heat exchanger between both states is used as the performance metric.
- **Interface Thermal Margin (TM)** Interface thermal margin is the percentage difference between interference fit and differential thermal growth, and represents the allowable deviation in thermal resistance or heat load before interface separation.
- **Assembly Differential** To assemble the core on the heat exchanger, the core must be heated and the heat exchanger cooled sufficiently as to produce at least 15 thou of clearance[¶] between heat exchanger OD and core ID during the assembly process. Assembly differential is defined as the combined temperature difference that must be applied (e.g. cooling the heat exchanger by 20°C and heating the core by 80°C for a combined assembly differential of 100°C). Increased assembly differentials will require different cooling approaches (e.g. switching from liquid CO_2 to liquid nitrogen), increasing cost and complexity of the assembly process. The core is limited to 200°C, at which the core plating will be pyrolyzed.

Increasing interference fit improves thermal margin at the cost of reduced structural safety factor and an increased assembly differential. The approach taken to select the design interference fit is as follows:

1) The temperature distribution of the core and heat exchanger during operation is estimated via the 2D thermal resistance network presented in Chapter 4.
2) The radial thermal growth of the core and heat exchanger is estimated separately via 2D thermal FEA using this temperature distribution as input. The core ID is estimated to grow by 9 thou and the heat exchanger ID to grow by 6 thou, yielding a differential thermal growth of 3 thou during operation.
3) Several candidate values of interference fit are selected and the performance metrics assessed via FEA of the core-heat exchanger assembly at both cold and operating states.
4) A nominal interference fit value is selected to ensure that all three performance metrics are satisfactory for that value and across a variation of ±1 thou (as the heat exchanger OD and core ID both have machining tolerances of +0/-1 thou).

[¶]The value of 15 thou is selected based on advice from individuals experienced with shrink fit assembly. Assembly is possible with reduced clearance values, but with an increased risk of the two components coming into contact during the process and becoming stuck.

A nominal interference fit of 5 thou is selected to balance the structural safety factor of the core and the risk of thermal separation. The performance metrics over the interference fit range are:

Interference Fit	Structural SF	Interface TM	Assembly Differential
6.0 thou	1.31	100 %	135°C
5.0 thou	**1.57**	**70 %**	**125°C**
4.0 thou	1.96	40 %	115°C

Table 1   Performance metrics across range of variation in interference fit, with selected nominal fit in bold

V. Experimental Validation of Heat Exchanger Performance

A. Torque Loading Experiment

A nondestructive evaluation of the heat exchanger's structural resilience is conducted, with the heat exchanger loaded to 112% of design torque repeatedly over five cycles to be sufficient for repeatability. Figure 14 presents a picture of the experiment setup and associated instrumentation. A 'dummy core' (hollow steel cylinder) is installed with an identical interference fit on the heat exchanger to replicate the compressive loading from the laminations in the demonstrator, and torque is exerted on the heat exchanger by means of a torque wrench loaded with weights on the end (Figure 15). Counter-torque is measured by load cells on either side of the torque drum, and angular deflection by a potentiometer connected to a lever arm on the other end of the shaft. As a safety measure, a stopper plate is attached to the shaft and will halt the shaft rotation by colliding with the bottom frame should the heat exchanger fail. The gap between the stopper plate and the frame is measured with pin gauges of 1-thou increments at each load step, and is used as a secondary measurement of the shaft angular deflection.
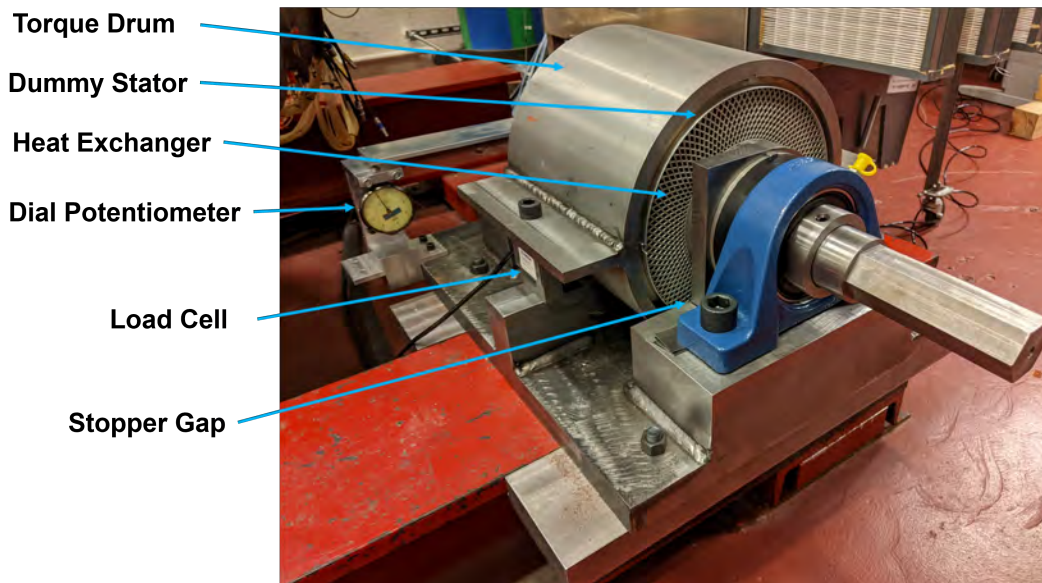

Fig. 14   Heat exchanger torque loading experiment setup and instrumentation

Figure 16 plots the estimated applied torque and measured counter-torque across all 5 loading cycles of 11 steps each. The two torques are in good agreement, showing that all torque is transferred through the heat exchanger. Figure 17 plots the shaft angular deflection calculated from the potentiometer and stopper gap measurements are repeatable and consistent across cycles. The angular deflection of stopper is hypothesized to be higher than that of the dial potentiometer due to the torsional deflection of the shaft. The heat exchanger and dummy core are examined after the experiment, and no damage to either component is observed.

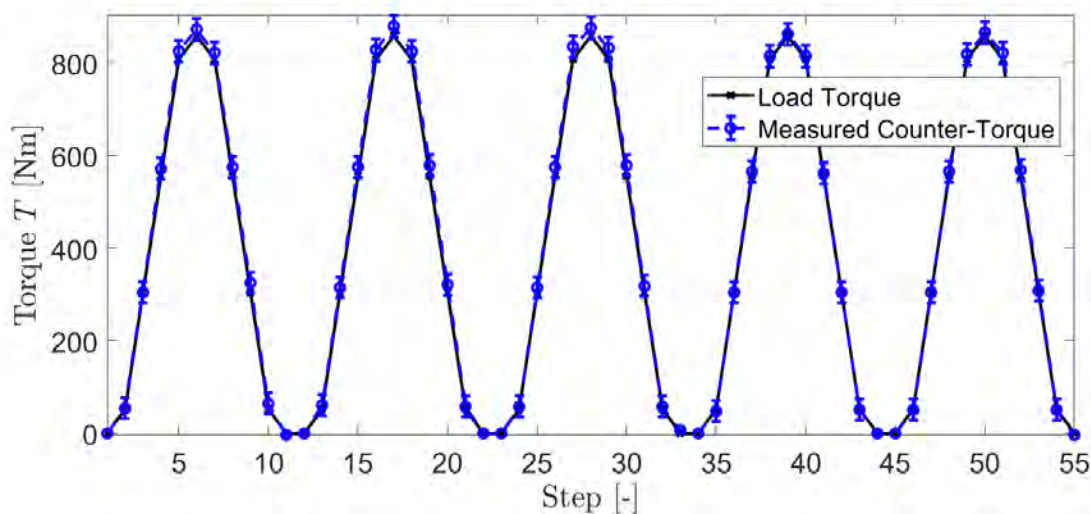**Fig. 15   Heat exchanger loaded to maximum of 857 Nm (112% design torque value of 765 Nm)**

Fig. 16   Applied torque and counter-torque in good agreement

B. Thermal Performance Characterization

A set of flow experiments are conducted on the heat exchanger to characterize its thermal resistance in conditions that match those in the final application as closely as possible. These measures include flow through the heat exchanger driven via suction produced by a downstream compressor, installation of the flow turner upstream of the heat exchanger, and applying heat on the surface of the dummy core (as the interfacial thermal resistance is considered part of the heat exchanger performance). Figure 18 presents the setup for the experiment, with the airflow following the arrows, and the locations of the flow sensors. The total pressure of the flow at the inlet to the 180 degree bend is measured with 3 probes in Plane 1, and the flow conditions immediately downstream of the heat exchanger characterized by a set of five probes - one temperature probe, one pitot-static probe, and three pressure probes measuring total pressure. These probes are shown in Figure 19. The exit flow is assumed to be axisymmetric, and the radial distribution of the exit flow properties characterized by taking measurements at multiple rake heights. Figure 20 illustrates the location of the temperature sensors on an 'unrolled' surface of the dummy core. The dummy core has two keyways (used to interface with the torque drum during the torque loading experiment). The orange rectangles represent the heating elements, and
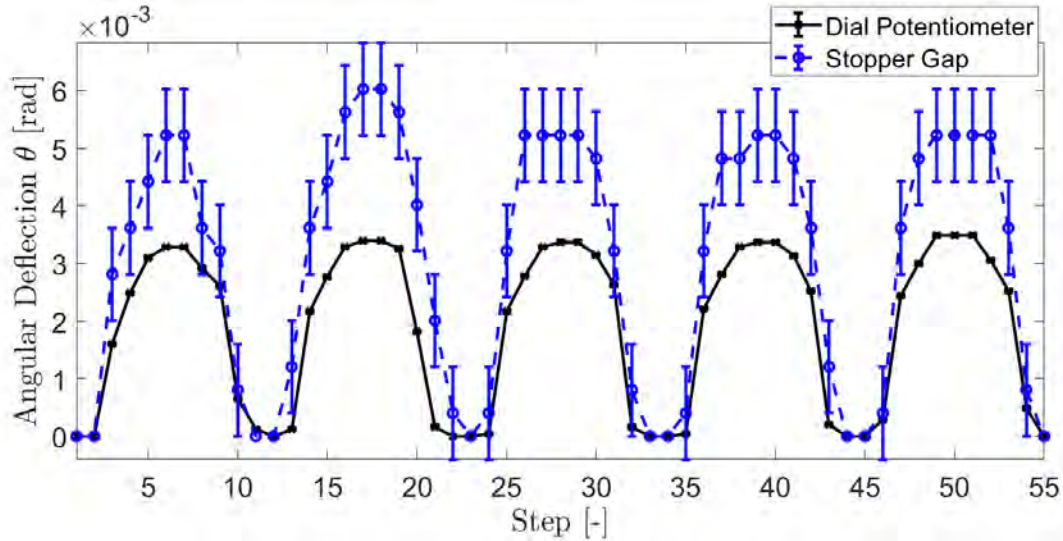
11

Fig. 17 Angular deflection estimates consistent across cycles

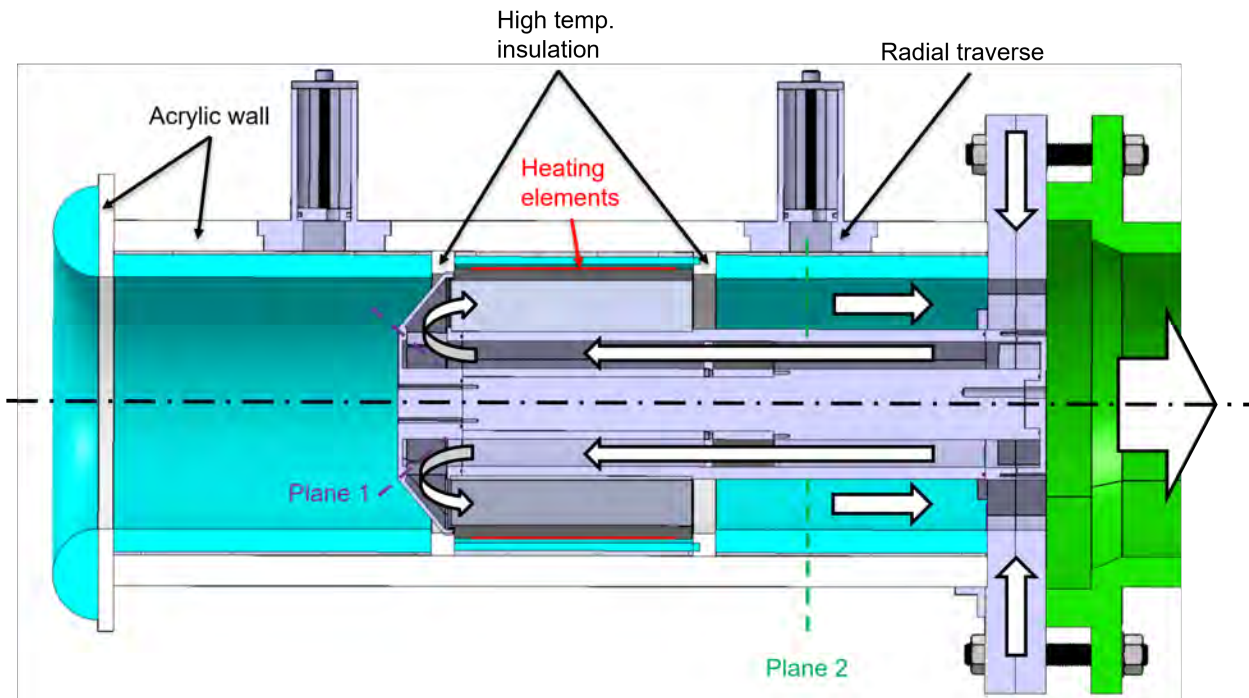the red dots the locations of temperature sensors.

Fig. 18 Cartoon illustrating flow experiment setup and sensor locations

The heat exchanger thermal resistance is defined as the difference between the maximum dummy stator inner surface temperature and the measured inlet air temperature divided by the input heat power. The thermal resistance of the dummy stator, constructed from 416 steel, is estimated at 0.0022 K/W. A total of six flow experiments encompassing all combinations of three mass flow rates and two heat loads were conducted. Experimental estimates of the heat exchanger thermal resistance are plotted against CFD estimates in Figure 21, found to align well. The heat exchanger thermal resistance of 0.0059 K/W at design mass flow conditions is 17% lower than the maximum allowed value of 0.0071 K/W, which meets the thermal requirement to maintain the winding hotspot temperature below 180°C.
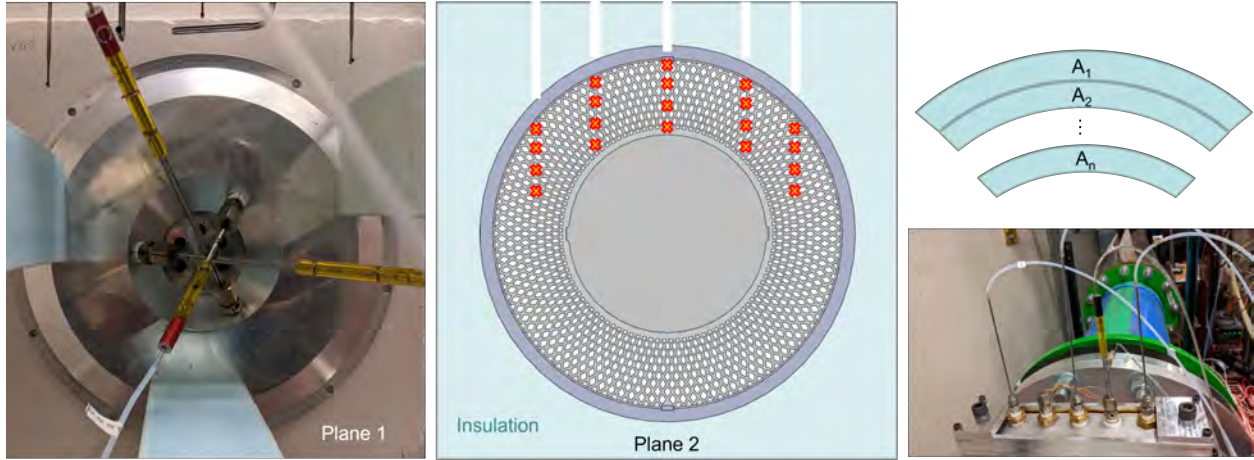
12

Fig. 19   Plane 1 probes (left), cartoon illustrating rake locations (middle), and flow probes in plane 2 (right)
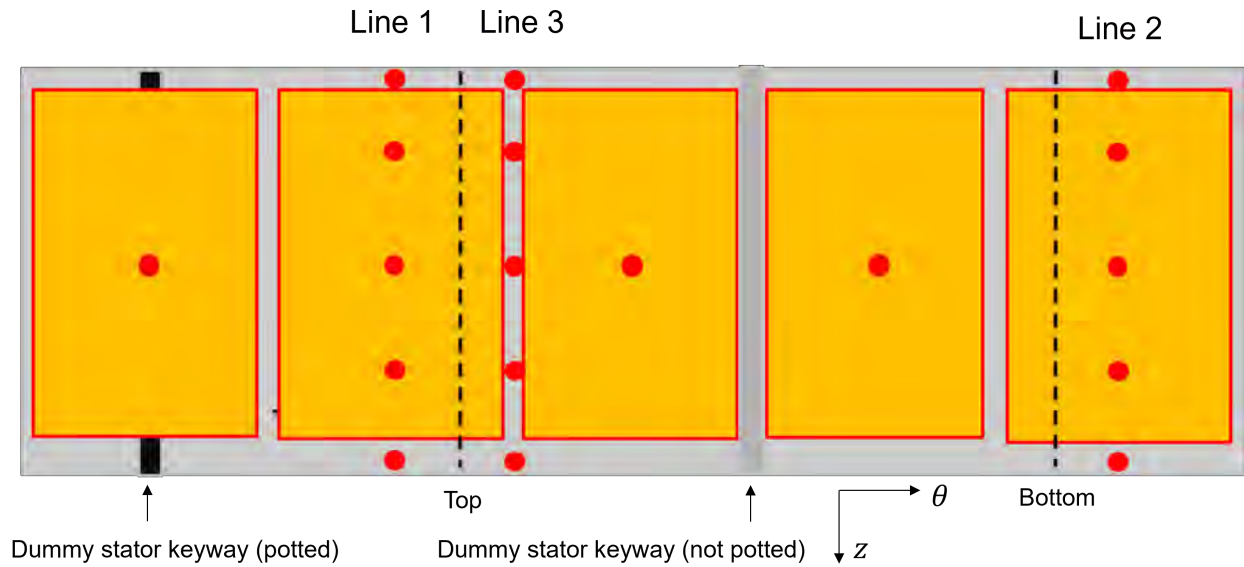

Fig. 20   Distribution of temperature sensors on outer surface of experimental heat exchanger

The pressure losses through the heat exchanger are characterized by an overall 'friction factor' $\lambda = \frac{\Delta p_t}{q_{in}}$, where the experimentally measured pressure losses are nondimensionalized by an estimated upstream mass-averaged channel inlet dynamic pressure. These losses include those incurred in the 180 degree bend and from the sudden contraction at the heat exchanger inlet and sudden expansion at the heat exchanger exit, and are thus expected to be higher than that predicted solely based on the channel surface roughness alone. Figure 22 plots this friction factor against the channel inlet Reynolds number $Re_{dH} = \frac{\rho u_{in} \bar{d}_H}{\nu}$, calculated from the mass-averaged channel inlet conditions estimated with the measured inlet total pressure, temperature, and downstream mass flow. The CFD results are of the heat exchanger with a uniform axial inlet flow, and an empirical loss coefficient for the bend losses is added to account for this missing component of the losses in the CFD. This loss coefficient is calculated from the interpolation of experimentally measured losses in the 180 degree bends. The experimentally measured pressure losses are found to match the CFD estimates well.

VI. Conclusion

As electric machine specific power improves and machines become more compact, the heat conduction path from source (windings, laminations) to cooling surface (heat exchanger) is reduced. This reduction in internal thermal
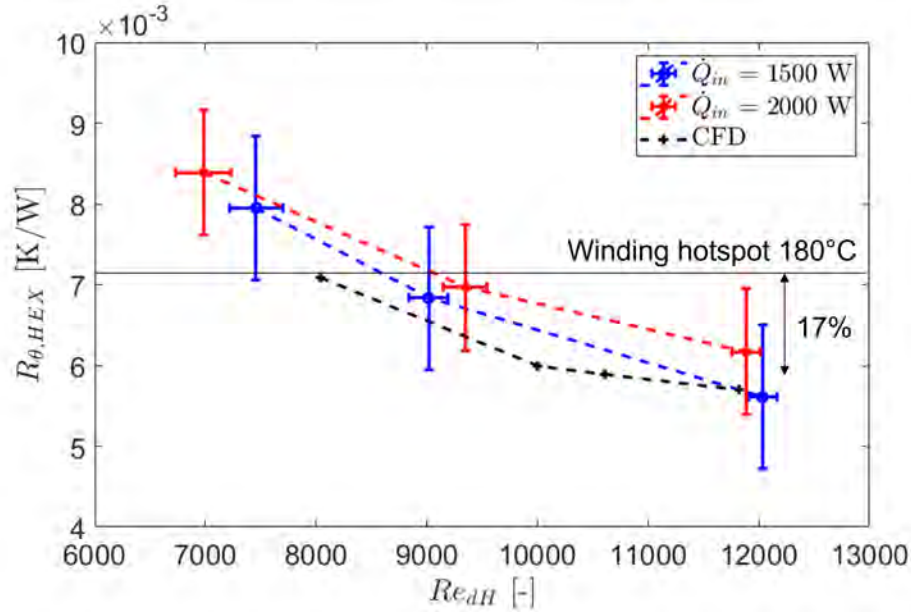
13

Fig. 21 Experimental estimates of heat exchanger thermal resistance align well with CFD estimates and meet results
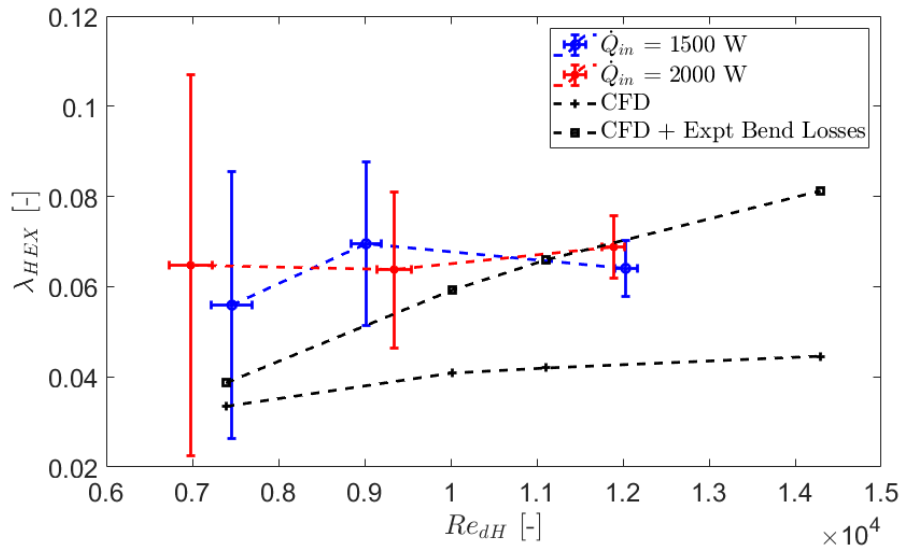

Fig. 22 Experimental estimates of heat exchanger friction factor match CFD results well, mitigating risk that design heat exchanger mass flow can be achieved

resistance alleviates the need for direct cooling (such as flowing coolant directly through the windings).

In exchange, the challenges associated with heat removal on the cooling surfaces are further amplified by the reduction in machine size. Increased heat flux exacerbates the differential thermal growth between the core and heat exchanger, and the associated challenges of preventing interface separation. An increase in torque density also increases the torsional stress in the heat exchanger. Taken together with the compression load of the interference fit, heat exchangers for future machine designs will require anti-buckling features such as that of the channel-type architecture.

Alternatively, the compressive loading from an interference fit could be mitigated by installing thermal pads between the heat exchanger and core. The thermal differential growth between core and heat exchanger would be absorbed by the

14

compressible thermal pads - in the cold (room temperature) state, this would reduce stresses in both the heat exchanger and core, while ensuring physical contact is maintained in operation. If the challenges associated with the installation process (risk of the core getting caught on the 'sticky' thermal pad) and vibrations in the machine stator due to the lack of a stiff connection between core and heat exchanger could be addressed, these pads may play a key role in future heat exchanger designs.

A reduced machine (and heat exchanger) size also reduces available coolant throughflow area. Without changing the coolant (air) and keeping flow velocity constant (due to pressure drop limitations), this results in a flow with lower Reynolds Number (and correspondingly Nusselt number and heat transfer coefficient). The ability to mitigate this loss in heat transfer coefficient by increasing cooling surface area with a larger number of smaller channels is strongly constrained by the acceptable pressure losses in the coolant flow. Predicting and managing surface roughness, a key parameter in the balance of heat transfer and pressure loss, in the thin-walled heat exchanger will be of critical importance.

Acknowledgments

References

[1] Bacellar, D., Aute, V., Huang, Z., and Radermacher, R., "Design optimization and validation of high-performance heat exchangers using approximation assisted optimization and additive manufacturing," *Science and Technology for the Built Environment*, Vol. 23, No. 6, 2017, pp. 896–911. https://doi.org/10.1080/23744731.2017.1333877, URL https://doi.org/10.1080/23744731.2017.1333877.

[2] Spakovszky, Z. S., Chen, Y., Greitzer, E. M., Cordero, Z. C., Lang, J. H., James L. Kirtley, J., Perreault, D. J., Andersen, H. N., Qasim, M. M., Cuadrado, D. G., Otten, D. M., and Amato, M., "A Megawatt-Class Electrical Machine Technology Demonstrator For Turbo-Electric Propulsion," AIAA/IEEE Electric Aircraft Technologies Symposium (EATS), 2023. Extended Abstract Submission.

[3] Hwang, J.-J., Hwang, G.-J., Yeh, R.-H., and Chao, C.-H., "Measurement of Interstitial Convective Heat Transfer and Frictional Drag for Flow Across Metal Foams ," *Journal of Heat Transfer*, Vol. 124, No. 1, 2001, pp. 120–129. https://doi.org/10.1115/1.1416690, URL https://doi.org/10.1115/1.1416690.

[4] Cheng, N.-S., "Formulas for Friction Factor in Transitional Regimes," *Journal of Hydraulic Engineering*, Vol. 134, No. 9, 2008, pp. 1357–1362. https://doi.org/10.1061/(ASCE)0733-9429(2008)134:9(1357).

[5] Wu, Z., Narra, S., and Rollett, A., "Exploring the fabrication limits of thin-wall structures in a laser powder bed fusion process," *International Journal of Advanced Manufacturing Technology*, Vol. 110, No. 2, 2020, pp. 191–207.

[6] Nikuradse, J., "Stromungsgesetze in Rauhem Rohren. (Laws of Turbulent Pipe Flow in Smooth Pipes.)," *VDI-Forschungsheft: Germany*, 1933, pp. 361. (Translated in NACA Tech. Memo. No. 1292, 1050).